

1 **Measurement report: Nocturnal subsidence behind the cold** 2 **front enhances surface particulate matter in the plain regions:** 3 **observation from the mobile multi-lidar system**

4 Yiming Wang^{1, 2}, Haolin Wang^{1, 2}, Yujie Qin^{1, 2}, Xinqi Xu^{1, 2}, Guowen He^{1, 2}, Nanxi Liu^{1, 2}, Shengjie
5 Miao^{1, 2}, Xiao Lu^{1, 2}, Haichao Wang^{1, 2, *}, Shaojia Fan^{1, 2, *}

6 ¹School of Atmospheric Sciences, Sun Yat-sen University, and Southern Marine Science and
7 Engineering Guangdong Laboratory (Zhuhai), Zhuhai, 519082, China

8 ²Guangdong Provincial Observation and Research Station for Climate Environment and Air Quality
9 Change in the Pearl River Estuary, Key Laboratory of Tropical Atmosphere-Ocean System (Sun Yat-sen
10 University), Ministry of Education, Zhuhai, 519082, China

11 *Correspondence to:*

12 *Haichao Wang (wanghch27@mail.sysu.edu.cn); Shaojia Fan (eesfsj@mail.sysu.edu.cn)*

13 **Abstract.** A multi-lidar system, mounted in a vehicle to monitor the profiles of temperature, wind, and
14 particle optical properties, was utilized to investigate the winter fine particulate matter (PM_{2.5}) pollution
15 from a vertical perspective, in four cities in China in winter 2018. We observed the enhancement of
16 surface nocturnal PM_{2.5} in two typical plain cities (Changzhou and Wangdu), which was attributed to the
17 subsidence of PM_{2.5} transported from upstream polluted areas, with the wind turning north and
18 downdrafts dominating. Combining with the observed surface PM_{2.5}, the reanalysis meteorological data,
19 and the GEOS-Chem model simulation, we revealed the Transport-Nocturnal PM_{2.5} Enhancement by
20 Subsidence (T-NPES) events occurred frequently in the two cities, with percentages of 12.2 % and
21 18.0 %, respectively during Dec. 2018 - Feb. 2019. Furthermore, the GEOS-Chem model simulation
22 further confirmed the ubiquity of winter T-NPES events on a large scale including North China Plain
23 and the Yangtze River Delta. Process analysis revealed that the subsidence was closely correlated with
24 the southeasterly movement of the high-pressure system and the passage of the cold front, resulting in
25 the increase of temperature aloft, a stronger inversion layer, and further PM_{2.5} accumulation in the
26 atmospheric boundary layer. Thus, a conceptual model of the T-NPES events was proposed to highlight
27 this surface PM_{2.5} enhancement mechanism in these plain regions. However, it did not apply to the two
28 cities in the basin region (Xi'an and Chengdu), due to the obstruction of the weather system movement
29 by the mountains surrounding the basin.

30 **1 Introduction**

31 The severe fine particulate matter (PM_{2.5}, particles with an aerodynamic diameter smaller than 2.5 μm)
32 pollution, caused by the rapid industrialization and urbanization in China (Guo et al., 2014; Huang et al.,
33 2014), has essential impacts on visibility, ecosystem, regional and global climates, and human health
34 (Yue et al., 2017; An et al., 2019; De Marco et al., 2019; Li et al., 2019b; Hao et al., 2021). To mitigate
35 the PM_{2.5} pollution, the government of China implemented the Air Pollution Prevention and Control
36 Action Plan in 2013 by strict emission controls (Gao et al., 2020). Despite the fact that the annual average
37 concentration of PM_{2.5} has significantly decreased (Ding et al., 2019; Li et al., 2019a; Zhang et al., 2019b;
38 Silver et al., 2020; Geng et al., 2021b), the PM_{2.5} levels in the majority of Chinese cities are still above
39 the World Health Organization target (WHO, 2021). Particularly, the issue of PM_{2.5} pollution remained
40 critical in the North China Plain (NCP) and Yangtze River Delta (YRD) in winter time (Peng et al., 2021;
41 Qin et al., 2021).

42 The formation mechanisms of PM_{2.5} pollution were complex especially in China (Guo et al., 2014; Xiao
43 et al., 2021b), such as the high emission intensity (Zhang et al., 2019b), the rapid chemical formation of
44 secondary particles owing to the gas phase and heterogeneous reactions (Wang et al., 2017; Lu et al.,
45 2019; Chen et al., 2020), and the interactions within the atmospheric boundary layer (ABL) (Ding et al.,
46 2013; Gao et al., 2016; Dong et al., 2017; Li et al., 2017). While the long-range transport also had
47 significant impacts on the PM_{2.5} pollution (Guo et al., 2014; Zhang et al., 2015; Huang et al., 2018). Cold
48 fronts, as a common synoptic circulation in winter, were usually favorable for the quick removal of the
49 locally accumulated pollutants in the NCP (Zhao et al., 2013; Gao et al., 2017), but conversely transport
50 the pollutants to the YRD through a long distance (Kang et al., 2019; Huang et al., 2020; Kang et al.,
51 2021). Zhou et al. (2023) indicated that the cold fronts could transport the precursors to the residual layer,
52 where the secondary pollution was rapidly driven to be generated and then exacerbate near-surface air
53 pollution as a result of the development of the daytime convective ABL. However, the above studies
54 have focused on the impact of the horizontally transported pollutants on the downstream regions after
55 the passage of the cold front. In comparison, few studies have been conducted on the variation in the
56 vertical direction of particulate matter in the ABL during the passage of the cold front.

57 The vertical mixing exchange process between layer has great impact on local air quality and the
58 subsidence motion is associated with the evolution of the inversion layer (Gramsch et al., 2014; Xu et
59 al., 2018; He et al., 2022). Zhang et al. (2022) reported that the PM_{2.5} concentration behind the cold front
60 increased due to the subsidence motion and inversion layer. Zhao et al. (2023) suggested that the frontal

61 downdrafts were an additional transport pathway in the nighttime to make a higher contribution to the
62 ground nitrate. Both of their studies were based on the model simulations, the observational evidence of
63 the subsidence behind the cold front and its impact on the nocturnal $PM_{2.5}$ enhancement events is still
64 lacking. Shi et al. (2022) reported one subsidence case of particulate matter during the passage of the
65 cold front over Wangdu, China in winter, which revealed that the subsidence was closely connected to
66 the enhancement of nocturnal $PM_{2.5}$.

67 To investigate the mechanisms of nocturnal $PM_{2.5}$ enhancement triggered by subsidence, the three-
68 dimensional spatial and temporal distribution is crucial. Many field observations of the vertical
69 distribution of particulate matter have been performed employing various methods such as tethered
70 balloons (Wang et al., 2021; Ran et al., 2022), airplanes (Wang et al., 2018; Fast et al., 2022), unmanned
71 aerial vehicles (Song et al., 2021; Dubey et al., 2022) and the meteorological towers (Li et al., 2022; Yin
72 et al., 2023). Lidar, as an active remote sensing device with high temporal and spatial resolution, has
73 been extensively employed in atmospheric detection to obtain the profile of particulate matter, wind, and
74 temperature. The ground-based and satellite-based lidar have been widely used to detect the vertical
75 distribution of aerosol. In recent years, the mobile multi-lidar system has been gradually developed and
76 has become a powerful tool for observing target species in a vertical perspective. Compared with the
77 traditional ground-lidar system, the mobile multi-lidar system enables continuous mobile observations
78 and provides information on the distribution of specific factors along its path and can be used as an
79 effective supplement to other fixed lidars. Additionally, the mobile multi-lidar system can reach different
80 cities by its portable setting in a short time to carry out fixed-point observations. The mobile lidar system
81 has been used to carry out several observations in the past few years (Lv et al., 2020; He et al., 2021; Xu
82 et al., 2022). He et al. (2021) investigated the vertical distribution characteristics of particulate matter in
83 the Guanzhong Plain by using the mobile multi-lidar system. Xu et al. (2022) conducted an observational
84 study on the three-dimensional structure of particulate matter distribution in the Guangdong-Hong Kong-
85 Macao Greater Bay Area by using the mobile multi-lidar system and proposed a conceptual model to
86 elucidate the vertical distribution of particulate matter under different wind and temperature conditions.
87 Here, we conducted the first nationwide field measurements in winter 2018 using the mobile multi-lidar
88 system during winter 2018 in China, to investigate the vertical distribution characteristics of particulate
89 matter in different cities. We focus on the observed nocturnal $PM_{2.5}$ enhancement events and seek insights
90 into their characteristics and causes, by combining with the GEOS-Chem model simulation, the surface
91 $PM_{2.5}$ observation, and meteorological reanalysis dataset. Finally, we examine the ubiquity of this

92 phenomenon in plain regions in China and propose a conceptual model, providing detailed vertical
93 insights into the enhancement of nocturnal surface PM_{2.5}.

94 **2 Data and methods**

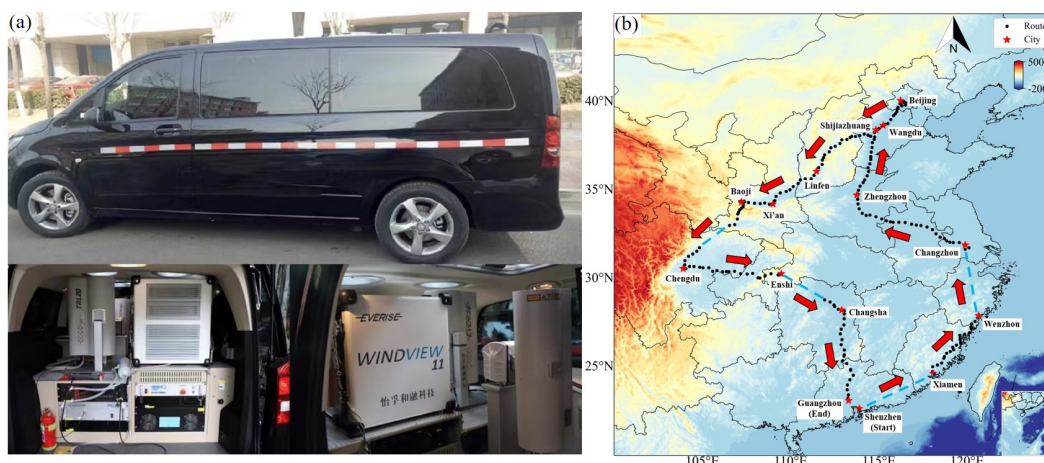
95 **2.1 Multi-lidar system**

96 A multi-lidar system was installed on the mobile observation vehicle. The vehicle, a modified 7-seater
97 Mercedes-Benz sport utility vehicle, was equipped with three lidar instruments mounted on steel bars at
98 the rear for stability. The mobile observation routes were primarily on flat highways, and the speed was
99 controlled to remain around 80 km/h to minimize the impact of frequent changes in speed and vehicle
100 bumps on the measurement results.

101 The multi-lidar system (Everise Technology Ltd., Beijing) consisted of a 3D visual scanning micro pulse
102 lidar (EV-Lidar-CAM), a twirling Raman temperature profile lidar (TRL20), a Doppler wind profile lidar
103 (WINDVIEW10), a global positioning system (GPS). The 3D visual scanning micropulse lidar had a
104 detection range of up to 30 km, a temporal resolution of 1 minute, and a vertical resolution of 15 m. The
105 3D lidar used an Nd: YAG laser to emit a 532 nm laser beam at a repetition frequency of 2500 Hz, which
106 is scattered by aerosol particles in the atmosphere. The backscattered signal is utilized to calculate the
107 aerosol extinction coefficient and depolarization ratio profile. The extinction coefficient increases with
108 higher particle pollution concentrations, while the depolarization ratio can distinguish between spherical
109 and non-spherical particles based on their size and shape. The Doppler wind profile lidar provides a
110 temporal resolution of 1 minute and a vertical resolution of 50 m. It emits a rotating 1545 nm laser beam
111 using a 10 kHz repetition rate fiber-pulse laser and measures the Doppler shift produced by the laser's
112 backscattered signal as it passes through airborne particles such as dust, water droplets in clouds and fog,
113 polluted aerosols, salt crystals, and biomass-burning aerosols to derive the horizontal and vertical wind
114 speeds at any height. The Raman temperature profile lidar, based on Raman scattering theory, calculates
115 atmospheric temperature by detecting the rotational Raman scattering signal of nitrogen or oxygen
116 molecules in the atmosphere. Operating at a 532 nm wavelength with an Nd: YAG laser at a repetition
117 frequency of 20 Hz, it has a temporal resolution of 5 minutes and a vertical resolution of 60 m. The
118 quality of the data obtained by the lidar system was checked by the Integrated Environmental
119 Meteorological Observation Vehicle before deployment. The results showed a percentage difference of
120 less than 15% between the lidar system data and the data provided by the Shenzhen Meteorological

121 Tower, demonstrating the high accuracy of the lidar instrument (Xu et al., 2022). Data during the
122 instrument malfunction, below the blind zone, and in rainy weather had been excluded. Previous studies
123 have utilized this lidar system and demonstrated its reliability (Xu et al., 2018; He et al., 2021). The
124 mobile observation vehicle and multi-lidar system are shown in Figure 1(a). The more details of the
125 multi-lidar system are shown in the Table S1.

126



127

128 **Figure 1.** (a) The mobile observation vehicle and multi-lidar system. (b) For the mobile observation route and
129 stopover cities, the blue dotted line shows the sections of missing data.

130 2.2 The route of nationwide mobile observation

131 To investigate the distribution characteristics of particulate matter during winter in different regions in
132 China, the Integrated Environmental Meteorological Observation Vehicle of Sun Yat-sen University was
133 utilized to conduct the first nationwide mobile observation campaign. The campaign, which lasted 43
134 days and covered approximately 11,000 km, started in Shenzhen on 30 November, 2018 and ended in
135 Guangzhou on 11 January, 2019. This campaign surveyed the PM_{2.5} vertical profiles across 15 cities,
136 including Shenzhen, Xiamen, Wenzhou, Changzhou, Zhengzhou, Wangdu, Beijing, Shijiazhuang,
137 Linfen, Xi'an, Baoji, Chengdu, Enshi, Changsha and Guangzhou. The observation route and stopover
138 cities are shown in Figure 1(b). Due to the precipitation, there were no observations between Shenzhen-
139 Xiamen and Wenzhou-Changzhou, while some GPS data were missing between Beijing-Chengdu and
140 Enshi-Changsha.

141 To compare the vertical distribution characteristics of particulate matter in different regions, we
 142 conducted fixed-point observations for several pollution days in four representative cities in the East
 143 China region (Changzhou), North China Plain (Wangdu), Guanzhong Basin (Xi'an), and Sichuan Basin
 144 (Chengdu). The dates and duration of the fixed-point observations are presented in Table 1. In the
 145 following analysis, only the data obtained in the four fixed-point measurements are used since it has
 146 enough time duration to show the vertical variation of PM_{2.5}.

147 **Table 1.** Date and cities of fixed-point observations

Date	Cities	Coordinate	Landform
2018.12.11-2018.12.14	Changzhou	119.97°E, 31.83°N	Plain area
2018.12.18-2018.12.22	Wangdu	115.25°E, 38.67°N	Plain area
2018.12.31-2019.01.02	Xi'an	109.01°E, 34.22°N	Basin area
2019.01.04-2019.01.09	Chengdu	103.92°E, 30.58°N	Basin area

148

149 **2.3 Surface PM_{2.5} data and ERA5 reanalysis data**

150 The nationwide hourly observations of surface PM_{2.5} in China are obtained from the China National
 151 Environmental Monitoring Center (CNEMC) network (<https://quotsoft.net/air>, last accessed: March 2nd,
 152 2023). Here, we used the hourly PM_{2.5} concentration data from the whole winter of 2018 (Dec. 2018 –
 153 Feb. 2019) and selected data from the closest monitoring station to show the change in surface PM_{2.5}
 154 concentration at the four observation sites.

155 The spatial distribution of daily average surface PM_{2.5} concentration is obtained from the TAP team
 156 (<http://tapdata.org.cn>), with a spatial resolution of 10 km. Based on machine learning algorithms and
 157 multi-source data information, the TAP team has built a multi-source data fusion system that integrates
 158 ground observation data, satellite remote sensing information, high-resolution emission inventories, air
 159 quality model simulations, and other multi-source information (Geng et al., 2021a; Xiao et al., 2021a).
 160 In addition to the observation data, we also apply the three-dimensional meteorological data from the
 161 ERA5 dataset for the winter of 2018 (<https://quotsoft.net/air>, last accessed: March 2nd, 2023) (Munoz-
 162 Sabater et al., 2021). This dataset contained temperature, horizontal and vertical wind speed, and
 163 direction at pressure levels, as well as two-dimensional data including sea-level pressure and 2-m
 164 temperature. The ERA5 dataset is the fifth generation of the European Centre for Medium-Range

165 Weather Forecasts (ECMWF) atmospheric reanalysis of the global climate. The ERA5 dataset has a
166 horizontal resolution of $0.25^{\circ} \times 0.25^{\circ}$, a vertical resolution of 25 hPa, and a temporal resolution of 1 h.

167 **2.4 HYSPLIT backward trajectory model**

168 The Hybrid Single Particle Lagrangian Integrated Trajectory Model (HYSPLIT) (Stein et al., 2015),
169 developed by NOAA Air Resources Laboratory, is a valuable tool for simulating the movement of air
170 mass and the transport of pollutants in the atmosphere, is used in our study to obtain the sources of
171 particulate matter at different heights. Altitudes of 100, 500, and 1000 m were set as the endpoints of the
172 trajectories, the meteorological input for the trajectory model was the FNL dataset, and each trajectory
173 was calculated for 24 h duration.

174 **2.5 GEOS-Chem model description**

175 Given the short-term (less than one week) fixed-point observation duration of the mobile observation
176 vehicle in each city, we employ the global three-dimensional chemical transport model GEOS-Chem
177 version 13.3.1 to interpret the vertical observations (available at
178 <https://github.com/geoschem/GCClassic/tree/13.3.1>, last assessed: March 2nd, 2023, (Bey et al., 2001))
179 and to simulate the distribution of particulate matter concentrations during winter 2018 in China. We
180 perform the nested-grid version of the GEOS-Chem simulation at a spatial of 0.5° (latitude) \times 0.625°
181 (longitude) resolution over East Asia ($60\text{-}150^{\circ}\text{E}$, $11^{\circ}\text{S}\text{-}55^{\circ}\text{N}$). The model has 47 vertical layers with 18
182 layers in the below 3 km. Boundary chemical conditions for the nested models are archived from a
183 consistent global simulation run at 4° latitude \times 5° longitude resolution. Meteorological input is from the
184 Modern-Era Retrospective analysis for Research and Application version 2 (MERRA-2) (Gelaro et al.,
185 2017). We conduct the model simulation from 2018/11-2019/02 with the first month as a spin-up.
186 The model mechanisms and emissions mostly follow our previous study (Wang et al., 2022). In short,
187 the GEOS-Chem model describes a comprehensive stratospheric and tropospheric ozone- NO_x -VOCs-
188 aerosol-halogen chemical mechanism (Wang et al., 1998; Park et al., 2004; Parrella et al., 2012; Mao et
189 al., 2013). Photolysis rates are computed using the Fast-JX scheme (Bian and Prather. 2002). Advection
190 of tracers in GEOS-Chem is accomplished through the TPCORE advection algorithm. The boundary
191 layer mixing process is described in (Lin and McElroy. 2010). Dry and wet deposition of both gas and
192 aerosols is considered (Wesely. 1989; Zhang et al., 2001). We apply the latest version of the Community
193 Emissions Data System (CEDSV2) anthropogenic emissions inventory (O'Rourke et al., 2021), in which

194 the emissions over China have been adjusted to align with the Multi-resolution Emission Inventory for
195 China (MEIC) inventory (Zheng et al., 2018). Figure S1 showed the comparison of model results with
196 observations for monthly mean $PM_{2.5}$, and the correlation coefficients between model and observation
197 were about 0.6, which meant that the model results provided a relatively good reproduction of the
198 observations.

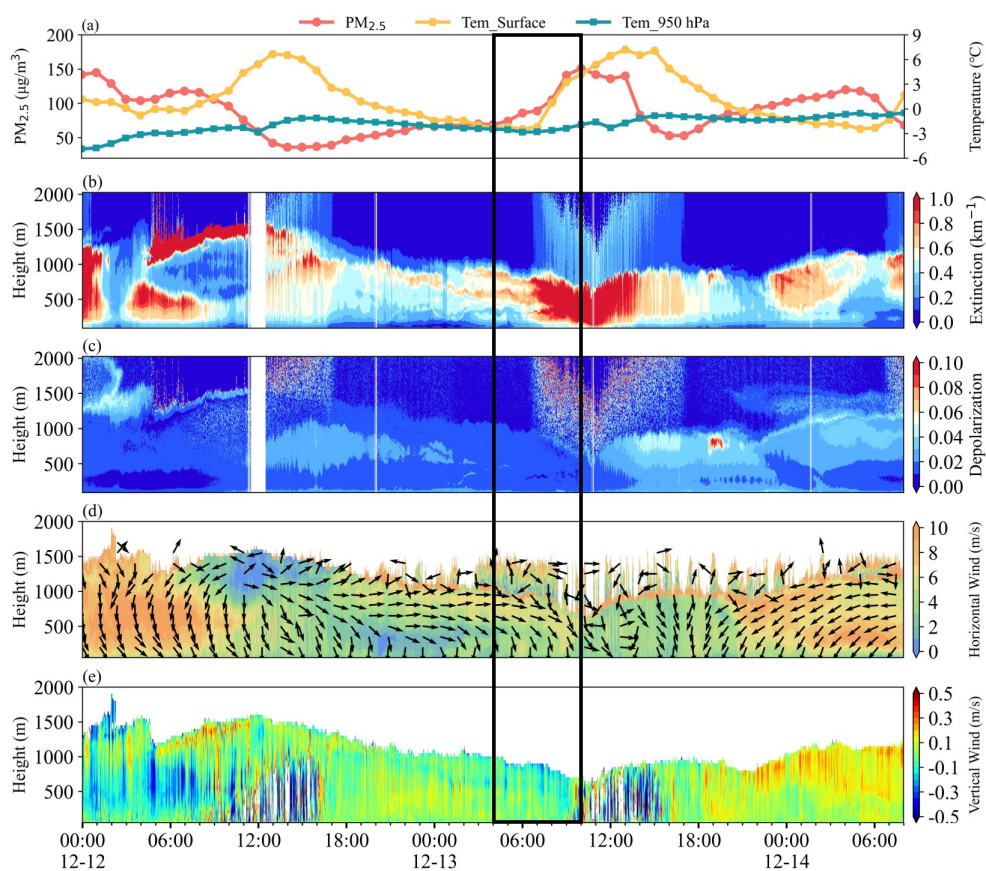
199 **3 Results and discussions**

200 **3.1 The observation of nocturnal $PM_{2.5}$ enhancement in plain areas**

201 During the fixed-point observation in Changzhou, we observed a typical surface $PM_{2.5}$ concentration
202 enhancement event starting at 4:00 and lasting until 10:00 on 13 December. As shown in Figure 2(a), the
203 concentration of $PM_{2.5}$ increased from 69 to 151 $\mu\text{g}/\text{m}^3$. Figure 2(b-c) shows the spatiotemporal
204 distribution of the extinction coefficient and depolarization ratio. There was a clear layer with a low
205 extinction coefficient below 500 m from 16:00 on 12 December to 4:00 on 13 December, indicating low
206 $PM_{2.5}$ concentration near the surface. Meanwhile, an aerosol layer with a high extinction coefficient of
207 about 0.7 km^{-1} appeared at 500-1,000 m. Figure 2(d-e) depicted the west winds prevailing in the layer of
208 500-1,000 m with a wind speed (WS) of about 7 m/s. Based on the daily average concentration of $PM_{2.5}$
209 on 12 December shown in Figure S2, the western area of the observation site in Changzhou suffered
210 from severe air pollution with the concentration of $PM_{2.5}$ exceeding $150 \mu\text{g}/\text{m}^3$. Under the strong forcing
211 of the west winds, the regional transport of aerosol from the west of Changzhou was detected, leading to
212 a high extinction coefficient layer at 500-1,000 m. The spatiotemporal distribution of the vertical velocity
213 in Figure 2(e) indicated the dominant updraft winds in the ABL, which was conducive to the suspension
214 of pollutants at 500-1,000 m.

215 However, the prevailing winds at 500-1,000 m shifted to the northwest/north after 4:00 on 13 December.
216 By 8:00, the north wind dominated in the ABL. The change in wind direction affected the transport
217 process of pollutants at 500-1,000 m, after which the transport basically disappeared. Meanwhile, the
218 downdraft winds dominated above 500 m (Figure 2(e)) and the aerosol layer suspended at 500-1,000 m
219 began to gradually transport and diffuse downward into the lower layer of ABL, which enhanced the
220 nocturnal surface $PM_{2.5}$ concentration. Noteworthy, after 4:00 on 13 December, the surface temperature
221 was close to the temperature at 950 hPa, suggesting that the structure of the ABL was stable and was
222 conducive to the accumulation of the $PM_{2.5}$.

223 The sea surface field showed the cold high-pressure system moved southeast with increasing strength
 224 from 20:00, 12 December to 8:00, 13 December (Figure S3). The change in the synoptic weather system
 225 was accompanied by a cold frontal passage. The cold frontal passage was inferred to start at about 4:00,
 226 13 December and last about 4 hours, which was further illustrated by the clockwise rotation of the
 227 horizontal wind from the ground to the upper layer (Shi et al., 2022) and the transition from updrafts to
 228 downdrafts, the observation site was located behind the cold front after 4:00 where the descending
 229 movements dominated. Under the influence of the subsidence, the pollutants transported by the west
 230 advection diffused downward to the low layer and further aggravated the local air quality.

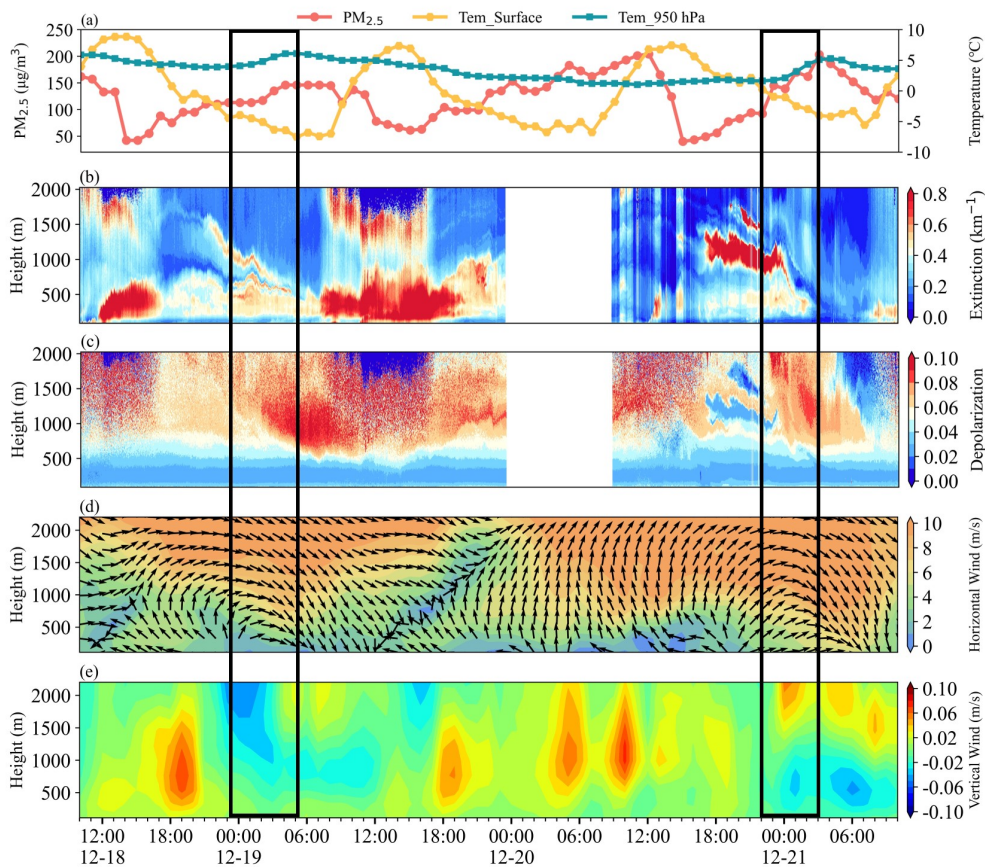


231

232 **Figure 2.** (a) Surface PM_{2.5} concentration, surface temperature, and 950 hPa temperature, (b) Extinction coefficient,
 233 (c) Depolarization ratio, (d) Horizontal wind, and (e) Vertical wind, during the observation in Changzhou from 12
 234 December to 14 December. The black box indicated the nocturnal surface PM_{2.5} enhanced event.

235 After 8:00, the concentration of surface $\text{PM}_{2.5}$ increased rapidly and peaked at around 10:00, the
236 extinction coefficient below 1,000 m also reached a high level with 1.0 km^{-1} at the same time and the
237 depolarization remained at about 0.01. The surface temperature began to rise and the convective ABL
238 developed rapidly, which enhanced the vertical mixing and resulted in the rapid increase in surface $\text{PM}_{2.5}$
239 (Zhou et al., 2023). And the north winds following the passage of the cold front dominated in the ABL
240 after 8:00, which could bring pollution from the NCP to the YRD (Kang et al., 2019; Huang et al., 2020).
241 Therefore, we attribute the increase in the concentration of surface $\text{PM}_{2.5}$ from 4:00 to 10:00 to the
242 combination of the subsidence behind the cold front before 8:00, vertical mixing caused by the
243 development of the convective ABL, and the transport by the north winds.

244 We also found similar nocturnal surface $\text{PM}_{2.5}$ enhancement events during the fixed-point observation in
245 Wangdu, on 19 December and 21 December respectively (Figure 3(a)). The concentration of $\text{PM}_{2.5}$
246 started to enhance at 1:00, 19 December, and meanwhile, the layer of pollutants above 1,000 m started
247 to transport and diffuse to the lower layer of ABL which was reflected by the change of the extinction
248 coefficient shown in Figure 3(b). Unfortunately, due to the instrument malfunction, the wind profile data
249 was unavailable and we used the ERA5 data instead, which previously showed good consistency with
250 the observation of with Doppler wind lidar (Shi et al., 2022). As shown in Figure 3(d), from 10:00, 18
251 December to 0:00, 19 December, southwest winds prevailed above 1,000 m and the WS exceeded 8 m/s,
252 a persistent southerly wind could result in severe air pollution in the NCP (Cai et al., 2017; Callahan et
253 al., 2019; Zhang et al., 2019a). The wind forced the regional advection of pollutants from the south region
254 suffering from serious air pollution (Figure S4) to the observation site. Meanwhile, the updrafts
255 dominated in the ABL which facilitated the suspension of pollutants in the upper layer. After 0:00, 19
256 December, as the cold high-pressure system moved southwest accompanied by a cold front (Figure S5),
257 the prevailing winds above 1,000 m shifted to the northwest gradually and downdrafts dominated behind
258 the cold frontal passage. The changes in the horizontal and vertical wind fields caused the advection of
259 pollutants to disappear basically and the pollutants layer suspended above 1,000 m began to transport
260 and diffuse downward to the low layer of ABL. The passage of the cold front at 0:00, 19 December,
261 lasted for 4 hours, and the subsidence behind the cold front caused the pollutants to diffuse downward,
262 enhancing the concentration of nocturnal $\text{PM}_{2.5}$.



263

264 **Figure 3.** (a) Surface PM_{2.5} concentration, surface temperature, and 950 hPa temperature, (b) Extinction coefficient,
 265 (c) Depolarization ratio, (d) Horizontal wind, and (e) Vertical wind, during the observation in Wangdu from 18
 266 December to 21 December. The black boxes indicated the Nocturnal PM_{2.5} enhancement events.

267 The pattern of the nocturnal surface PM_{2.5} enhancement event on 21 December was highly similar to that
 268 on 19 December. However, the pollutant advection process lasted a longer duration which started at
 269 16:00, 20 December and ended at 0:00, 21 December (Figure 3(b)), and the WS of the southwest wind
 270 above 1,000 m exceeded 12 m/s meeting the standard of the low-level jet (LLJ) (Kraus et al., 1985; Hu
 271 et al., 2013). The area south of the observation site in Wangdu suffered from more severe air pollution
 272 with the concentration of PM_{2.5} exceeding 300 $\mu\text{g}/\text{m}^3$ (Figure S6). Under the strong forcing of the
 273 southwestern LLJ and the updrafts depicted in Figure 3(d-e), an aerosol layer with high extinction
 274 coefficient exceeding 2 km^{-1} formed and was suspended at 1,000-1,500 m from 16:00, 20 December to

275 0:00, 21 December. Meanwhile, Figure 3(c) showed that the layer with low depolarization was consistent
276 with the layer with a high extinction coefficient, further confirming the role of transportation.

277 After 0:00, the wind direction of LLJ began to change due to the southeasterly movement of the high-
278 pressure system accompanied by a cold front (Figure S7). The passage of the cold front started at 0:00,
279 21 December, and lasted for 4 hours, after which the downdrafts dominated below 1,500 m (Figure 3(e)),
280 and the northwestern LLJ no longer transported pollutants from the southern area but greatly enhanced
281 the turbulent mixing (Shi et al., 2022). Under the influence of the turbulence generated by LLJ and
282 subsidence behind the cold front, the aerosol-rich layer suspended at 1,000-1,500 m was gradually
283 transported and diffused downward into the lower layer of ABL, ultimately enhancing the concentration
284 of surface $PM_{2.5}$, which was consistent with the result reported by Shi et al. (2022), with the secondary
285 inorganic aerosol increasing simultaneously during the subsidence process as observed by the tethered
286 balloon.

287 Noteworthy, when both nocturnal surface $PM_{2.5}$ enhancement events in Wangdu occurred, the
288 temperature at 950 hPa showed an increasing trend as a result of the heating of the air by compression as
289 it descended, while the surface temperature continuously declined (Figure 3(a)). The opposite variation
290 of surface temperature and temperature at 950 hPa stabilized the lower atmosphere. The stronger
291 inversion layer was probably induced by subsidence (Carlson and Stull. 1986). With the more stable
292 atmospheric layer and inversion during subsidence, the concentration of surface $PM_{2.5}$ enhanced
293 (Gramsch et al., 2014; Largeron and Staquet. 2016).

294 **3.2 Transport-Nocturnal $PM_{2.5}$ Enhancement by Subsidence Events**

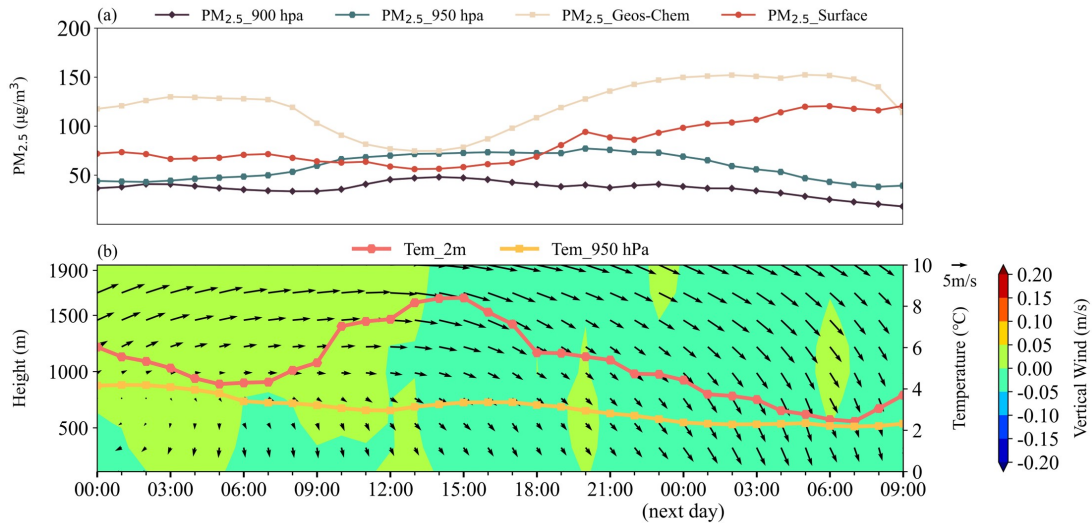
295 During the fixed-point observation, we found the causes of three nocturnal $PM_{2.5}$ enhancement events in
296 different cities were similar. The processes can be summarized as three steps: First, the horizontal winds
297 with high wind speed forced the transport of pollutants from the upstream region, while the updrafts
298 dominated, resulting in the formation and suspension of an aerosol layer with high extinction coefficient
299 at the high layer of the ABL. Then, under the influence of the southeasterly movement of the high-
300 pressure system and the passage of the cold front, the horizontal wind direction shifted to the north or
301 northwest and the downdrafts became dominant. Finally, the transport of pollutants disappeared due to
302 the change of wind direction, and under the subsidence behind the cold front, the aerosol-rich layer
303 suspended at the high layer was gradually transported and diffused downward into the lower layer of the

304 ABL, ultimately enhancing the concentration of nocturnal $PM_{2.5}$. Here, we defined this pollution pattern
305 as T-NPES (Transport-Nocturnal $PM_{2.5}$ Enhancement by Subsidence) events.

306 To investigate the occurrence frequency of T-NPES events, we employed the GEOS-Chem model to
307 simulate the distribution of particulate matter concentrations in China during the whole winter of 2018
308 (Dec. 2018 – Feb. 2019). We utilized the simulated $PM_{2.5}$ at 950 hPa and 900 hPa to represent the high-
309 altitude $PM_{2.5}$ concentration. We selected the closest grid data of the wind field data, 950 hPa, and 2-m
310 temperature data from the ERA5 dataset to the observation site in Changzhou and Wangdu to show the
311 meteorological condition. By analyzing the hourly concentration variation of $PM_{2.5}$ and the distribution
312 of the wind field during the three months of winter 2018 in Changzhou and Wangdu, we found 11 typical
313 T-NPES events in Changzhou accounting for 12.2% and 18 T-NPES events in Wangdu accounting for
314 18%, which indicated that the T-NPES events were a relatively common phenomenon in the two cities.

315 Figure 4 shows the average pattern of all T-NPES events in Changzhou, the trend of the simulated $PM_{2.5}$
316 was consistent with the observation, confirming the credibility of the simulations. As shown in Figure
317 4(a), the enhancement of nocturnal surface $PM_{2.5}$ started at 21:00, when there was no significant
318 enhancement in anthropogenic $PM_{2.5}$ emissions, while the high-altitude $PM_{2.5}$ represented by $PM_{2.5}$ at
319 900 hPa and 950 hPa started to decrease, which was consistent with the observed event in Changzhou
320 described in Section 3.1. According to the distribution of the wind field (Figure 4(b)), west winds with
321 high wind speed prevailed in the layer above 1,000 m from 0:00 to about 18:00, which was conducive to
322 the transport of pollutants. The updrafts dominated from 0:00 to 12:00, forcing the pollutants suspending
323 in the upper layer, which was reflected by the enhancing $PM_{2.5}$ concentration at high altitude (Figure
324 4(a)). Despite the downdrafts dominating after 12:00, there was no immediate reduction in $PM_{2.5}$
325 concentration at high altitudes, which might be related to the fact that the horizontal wind direction had
326 not changed, and the transport of pollutants continued. A brief updraft before 21:00 suspended the
327 pollutants at high altitudes. After 21:00, northwester winds and downdrafts dominated in the ABL and
328 the high-altitude $PM_{2.5}$ began to gradually transport and diffuse downward causing the enhancement of
329 surface concentration of $PM_{2.5}$, and this process continued until 4:00 in the next day. The surface
330 temperature and the temperature at 950 hPa gradually approached, which is consistent with the observed
331 case in Changzhou, indicating that the structure of the ABL was stable and was conducive to the
332 accumulation of the $PM_{2.5}$. As shown in Figure S8, the average sea level pressure indicated that the
333 southeasterly movement of the high-pressure system and the passage of the cold front, which resulted in

334 the shift in wind direction and subsidence behind the cold front, were the main causes of the T-NPES
 335 events.

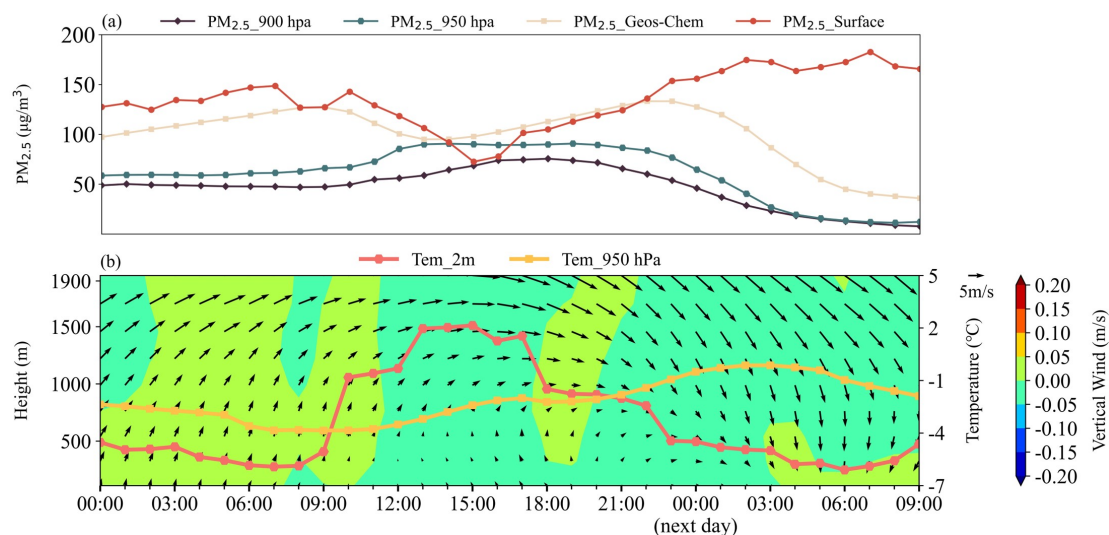


336

337 **Figure 4.** The average for all T-NPES events in Changzhou. (a) The concentration of PM_{2.5} at different levels,
 338 surface PM_{2.5} of observation (red line), surface PM_{2.5} of simulation (blue line), and PM_{2.5} at 900 hPa and 950 hPa.
 339 (b) The horizontal winds (arrows), the vertical winds (shaded), the temperature at 2 m, and temperature at 950 hPa.

340 Figure 5 shows the average pattern of all T-NPES events in Wangdu, which was similar to that in
 341 Changzhou. Figure 5(a) demonstrated that the trend of simulated PM_{2.5} was consistent with the
 342 observation before 22:00 but was different thereafter. The trend of high-altitude PM_{2.5} was increasing
 343 before 15:00 due to the transport of pollutants by prevailing southwester horizontal winds and the
 344 dominance of updrafts which suspended the aerosol shown in Figure 5(b). After 18:00, the prevailing
 345 winds began to turn northwest and ultimately turn north at 0:00 in the next day, while a brief updraft
 346 between 18:00 and 20:00 suspended the pollutants at high altitude. The ABL was dominated by the
 347 northwestern winds and downdrafts after 21:00. Simultaneously, the high-altitude PM_{2.5} began to
 348 gradually transport and diffuse downward causing the enhancement of surface concentration of PM_{2.5}.
 349 The temperature at 950 hPa increased and the surface temperature declined (Figure 5(b)), which agreed
 350 with the two observation examples in Wangdu. The opposite variation of temperature at different heights
 351 stabilized the ABL and further enhanced the concentration of PM_{2.5}. By analyzing the weather circulation
 352 patterns, the causes of the T-NPES events were the same as those in Changzhou and were attributed to
 353 the southeasterly movement of the high-pressure system and the passage of the cold front (Figure S9).

354 Overall, the average patterns of T-NPES events in Changzhou and Wangdu were essentially in good
 355 agreement with the three cases of T-NPES in the two cities. But there were still slight differences, such
 356 as the change of Wangdu caused by the movement of high-pressure lasted a longer time in the average
 357 situation and the start time of subsidence behind the cold front was also not consistent, which were due
 358 to each T-NPES event was not exactly the same.



359
 360 **Figure 5.** The average for all T-NPES events in Wangdu. (a) The concentration of PM_{2.5} at different levels, surface
 361 PM_{2.5} of observation (red line), surface PM_{2.5} of simulation (blue line), and PM_{2.5} at 900 hPa and 950 hPa. (b) The
 362 horizontal winds (arrows), the vertical winds (shaded), the temperature at 2 m, and temperature at 950 hPa

363 3.3 The universality of T-NPES events in eastern China

364 Despite the mobile observation vehicle had no observations in other cities of the NCP, the YRD, and the
 365 Loess Plateau, we could still utilize the simulated data and the ERA5 data to investigate the universality
 366 of T-NPES events occurrence in other cities. We selected Shijiazhuang, Beijing, and Tianjin as
 367 represented cities of the NCP, Shanghai, and Nanjing as represented cities of the YRD, and Taiyuan,
 368 Linfen as represented cities of the Loess Plateau. We found a similar pattern of T-NPES events in all
 369 these cities. However, these T-NPES events in different cities had some differences in detail. Here we
 370 divided the T-NPES events into four types based on the status of PM_{2.5} after T-NPES events. More
 371 information on the types, frequency of the T-NPES events, and their percentage of the winter 2018 was
 372 shown in Table 2.

373 The typical representation of Type 1 is shown in Figure S10, the characteristic of Type 1 was that the
 374 southwestern winds transported the pollutants in the high-altitude of the ABL, then the wind direction
 375 shifted to north and downdrafts dominated, finally, pollutants in high-altitude diffused into lower layer
 376 causing the surface PM_{2.5} enhanced. However, after the T-NPES event, the north wind near the ground
 377 was not strong enough to remove the pollutants, causing a high level of PM_{2.5} lasting the next day
 378 morning and may result in aggravation of the air pollution in the following day. The characteristic of
 379 the T-NPES event of Type 2 was basically consistent with Type 1. However, after the T-NPES event, as
 380 north winds became stronger, pollutants were rapidly removed, resulting in a clean boundary layer
 381 throughout (Figure S11). Even when the pollutants were removed more quickly by stronger north winds,
 382 the subsidence process might not be observed. Type 1 and Type 2 were both observed in the NCP cities,
 383 while Type 1 predominated in Wangdu and Shijiazhuang, and Type 2 in Beijing and Tianjin.

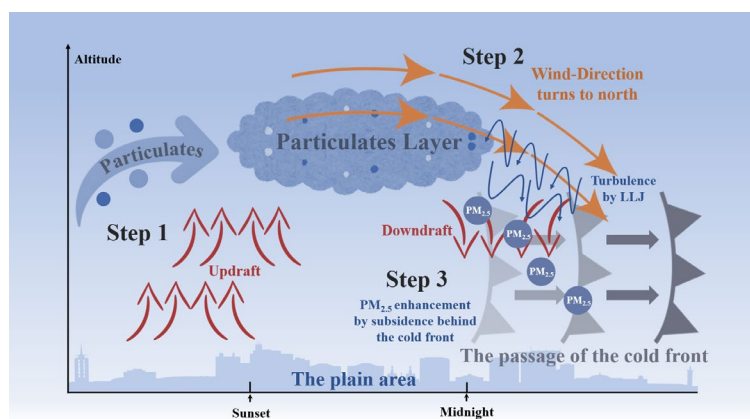
384 **Table 2.** Statistics of the T-NPES events in cities during Dec. 2018 – Feb. 2019

Area	Type	City	Frequency (days)	Percentages
NCP	Type 1 and 2	Wangdu	18	20.0%
		Shijiazhuang	18	20.0%
		Beijing	13	14.4%
		Tianjin	14	15.6%
YRD	Type 3	Changzhou	11	12.2%
		Shanghai	7	7.8%
		Nanjing	8	8.9%
Loess Plateau	Type 4	Linfen	18	20.0%
		Taiyuan	13	14.4%

385
 386 Figure S12 shows the typical representation of Type 3. The prevailing wind transporting pollutants was
 387 not southwest but west and the start and end of the T-NPES event were later than for Type 1 and 2. After
 388 the T-NPES event, the increase of 2-m temperature and the development of convective ABL led to
 389 vertical mixing and the increase of surface PM_{2.5}. Additionally, the stronger north wind might transport
 390 the pollutants from the NCP to the YRD. Type 3 was similar to the example in Changzhou in Section 3.1
 391 and indicative of a typical pattern in the YRD cities.

392 The typical representation of Type 4, which mainly occurred in the Loess Plateau cities, was shown in
393 Figure S13. During the T-NPES event, the change of wind direction was only observed above 1,500 m
394 while the wind speed below was so weak that the shift in wind direction was not significant, which was
395 significantly different from the wind field of the other three types. The reason for the difference between
396 Type 4 and other types was mainly related to the topography of the Loess Plateau, which has a blocking
397 effect on the movement of the high-pressure system. Noteworthy, after the analysis of these T-NPES
398 events in different cities in China, we suggested that the T-NPES events were a common pattern of the
399 nocturnal $PM_{2.5}$ enhancement, but did not always have an impact on the air pollution of the following
400 day. The pollution levels on the following day depended more on the strength of the cold front, local
401 pollution conditions, the structure of ABL, and regional transportation. Further quantification is needed
402 to determine the relationship between the T-NPES events and the pollution levels on the following day.
403 To look insights into the mechanism of nocturnal $PM_{2.5}$ enhancement, we systematically documented
404 instances of nocturnal $PM_{2.5}$ enhancement during the winter of 2018 in Wangdu and Changzhou
405 according to the surface $PM_{2.5}$ observation. We identified 48 such events in Wangdu and 27 in
406 Changzhou, with proportions of T-NPES events of 37.5% and 40.7%, respectively. The results implied
407 that T-NPES represents merely one among multiple pathways contributing to the nocturnal $PM_{2.5}$
408 enhancement. We checked the nocturnal $PM_{2.5}$ enhancement events that were not caused by T-NPES in
409 Wangdu, the dominant wind field distributions within the ABL were southerly or characterized by static
410 light wind, which indicated that the nocturnal $PM_{2.5}$ enhancement might result from either horizontal
411 transport from polluted regions in the southern areas or the local accumulation of particulates in the stable
412 ABL. In the nocturnal $PM_{2.5}$ enhancement events of non-T-NPES conditions in Changzhou, higher wind
413 speeds in the ABL and predominantly from the northern and southwestern, which indicated the nocturnal
414 $PM_{2.5}$ enhancement might result from horizontal transport from the NCP (Huang et al., 2020) or caused
415 by other reasons. For example, from the perspective of chemical formation, the nocturnal atmospheric
416 oxidation may elevate the nighttime aerosol concentration (Wang et al., 2023; Yan et al., 2023). In
417 addition, we found the T-NPES event does not always cause a nocturnal $PM_{2.5}$ increase, in a few cases,
418 the strong north wind following the cold front play a role in removing the aerosol. In summary, the T-
419 NPES just represents one vertical transport mechanism that can collectively contribute to the
420 enhancement of nocturnal $PM_{2.5}$ with other physical and chemical processes (Zhao et al., 2023). Further
421 understanding of the coupling effect of transportation as well as the chemical formation to the nocturnal
422 $PM_{2.5}$ enhancement is thus highly needed. Based on these mentioned above, we suggested that the T-

423 NPES events were a common phenomenon in winter in plain areas such as the NCP and the YRD. A
 424 conceptual model was thus developed and shown in Figure 6, there was the transportation of aerosol by
 425 the horizontal winds in the high altitude and the updrafts dominated before night, which was conducive
 426 to the formation and suspension of the aerosol layer. Then, with the southeasterly movement of the high-
 427 pressure system and the passage of the cold front at about the time of midnight, the wind direction began
 428 to turn north/northwest, causing the aerosol to dilute. Finally, the downdrafts dominated in the ABL and
 429 the LLJ might enhance the turbulence. Under the influence of subsidence behind the cold front and
 430 turbulence, the depth of the aerosol layer suspended in the high altitude began to decrease and the
 431 pollutants gradually transported and diffused downwards into the lower layer of the ABL, enhancing the
 432 concentration of surface $PM_{2.5}$.

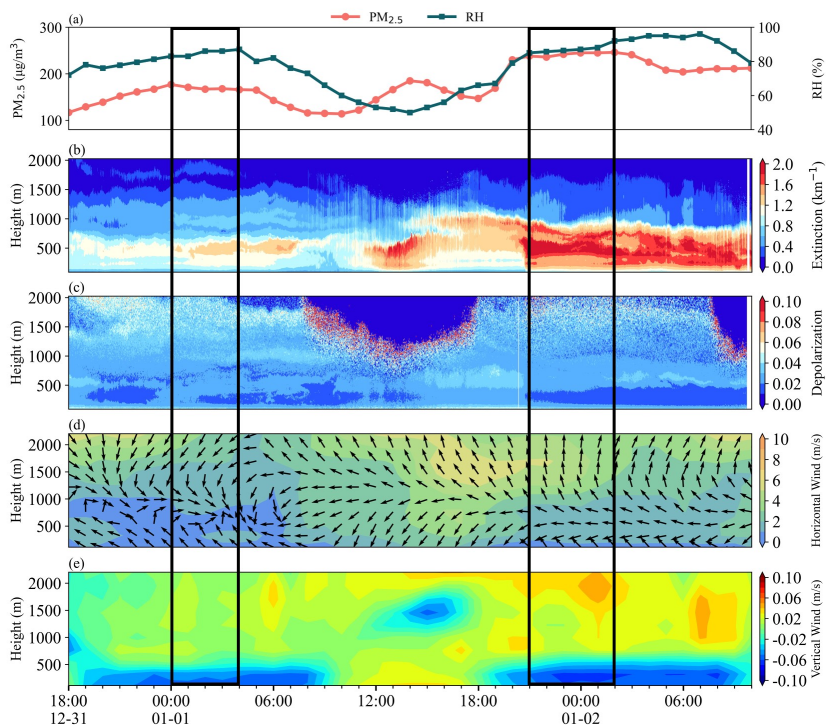


433
 434 **Figure 6.** Conceptual scheme of the T-NPES events

435 3.4 No T-NPES event occurred in Basin areas

436 We further checked the fix-point measurement in Xi'an and Chengdu, two cities with typical basin
 437 topography. The results indicated that there were essentially no T-NPES events in either city, suggesting
 438 the concept did not work. Figure 7(a) indicated that the concentration of surface $PM_{2.5}$ had no
 439 enhancement during the night from 23:00 on 31 December to 4:00 on 1 January, and from 22:00 on 1
 440 January to 3:00 on 2 January in Xi'an. $PM_{2.5}$ remained at a high concentration, while the extinction
 441 coefficient did not show the subsidence process, suggesting that the T-NPES events were not common
 442 here.

443 Taking the night of 31 December as an example, from 18:00 on 31 December to 4:00 on 1 January, the
 444 concentration of surface $\text{PM}_{2.5}$ increased before 23:00. Then it stabilized at high values, while the
 445 extinction coefficient remained at a high level with about $1.0\text{-}1.2\text{ km}^{-1}$ near 500 m. As shown in Figure
 446 7(d), from 18:00, 31 December to 6:00, 1 January, a light wind layer appeared below 1,000 m, with ~ 1
 447 m/s. Such a static and stable condition was conducive to the accumulation of locally generated particulate
 448 matter near the ground, causing the concentration of $\text{PM}_{2.5}$ to enhance between 18:00 and 23:00 on 31
 449 December and the formation and maintenance of the aerosol layer at about 500 m. Noteworthy, the wind
 450 direction at the low layer was southeaster, while it was the opposite northwester at about 1,000 m, which
 451 was the typical characteristic of mountain-valley breeze circulation. The dominance of downdrafts below
 452 500 m suggested that Xi'an was in the upper area of the nocturnal mountain-valley breeze circulation.
 453 The mountain-valley breeze circulation could only be observed when the background WS was relatively
 454 weak, which further indicated a stable structure of the ABL. The example on 1 January was similar to
 455 the above one, with the extinction coefficient reaching 2 km^{-1} and the depolarization ratio decreasing
 456 after 21:00 due to the hygroscopic growth of aerosol by the rise in relative humidity.



457

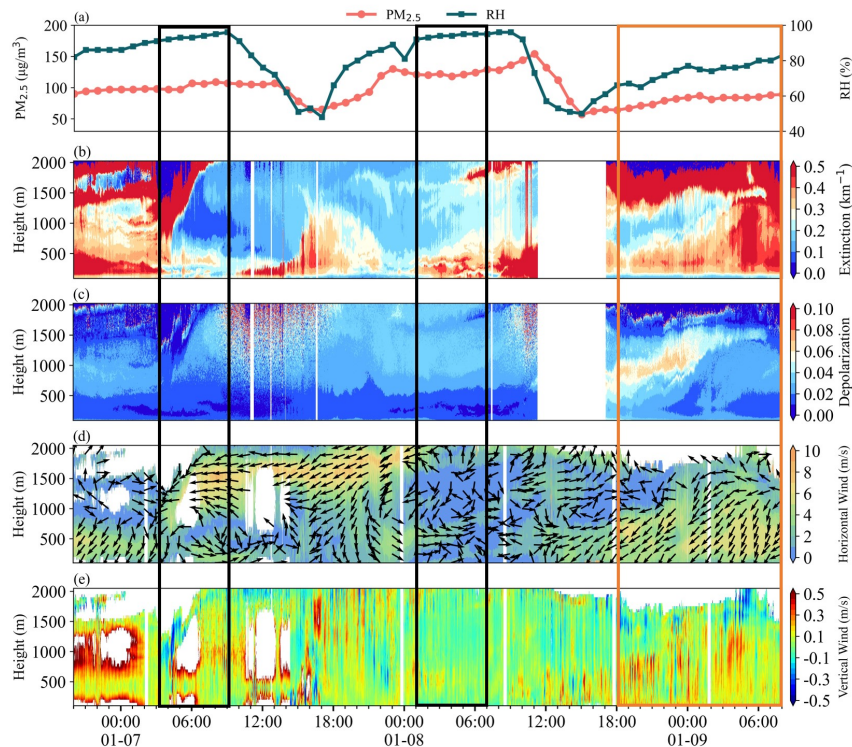
458 **Figure 7.** (a) Surface PM_{2.5} concentration and relative humidity, (b) Extinction coefficient, (c) Depolarization ratio,
459 (d) Horizontal wind, and (e) Vertical wind, during the observation in Xi'an from 18:00, 31 December to 10:00, 2
460 January. The two black boxes were the period to be studied.

461 Due to the topography of the basin in Xi'an, the mountain-valley breeze circulation, or the horizontal
462 winds with lower WS always dominated the ABL, which was not conducive to the transport and
463 dispersion of particulate matter. The stable structure of the ABL resulted in the particulate matter
464 accumulating in the low layer, which was the main feature of the nocturnal particulate matter distribution
465 in Xi'an.

466 Figure 8 showed that the concentration of surface PM_{2.5} also had no significant enhancement but
467 remained a high value over nighttime in Chengdu. The distribution of the extinction coefficient in the
468 two black boxes presented a double-layer structure, one layer near 250 m and another layer suspended at
469 about 500 m. Meanwhile, the wind field exhibited typical mountain-valley breeze circulation, as shown
470 in the two black boxes in Figure 8(d), which presented westerly wind near 250 m and southeasterly wind
471 above 500 m. The variation in wind direction due to the mountain-valley breeze circulation at different
472 layers might be responsible for the double layer of particulate matter. Figure S14 illustrates the backward
473 trajectories when the double-layer appeared. The layer of particulate matter at about 100 m might have
474 originated from the southwest area of Chengdu, whereas the layer of particulate matter at 500 m and
475 1,000 m might have originated from the northeast area of Chengdu. The different sources of particulate
476 matter were consistent with the mountain-valley breeze circulation in Chengdu, further demonstrating
477 the dominance of the mountain-valley breeze in the static and stable ABL at night.

478 The orange box in Figure 8 indicated that the distribution of particulate matter in the ABL of Chengdu
479 under the dominance of northeasterly winds with high WS. Both the extinction coefficient and the
480 depolarization ratio showed a stratified structure, with the extinction coefficient initially higher below
481 750 m and lower above 750 m, whereas the depolarization ratio exhibited the opposite trend. The main
482 cause of this phenomenon was that the different sources of particulate matter in the two layers. Under
483 the influence of the dominant updrafts, local emissions with a high depolarization ratio were transported
484 upwards, while the lower layer was occupied by particulate matter with a lower depolarization ratio
485 transported by the northeasterly wind. As the continuous transport of the northeasterly wind, the entire
486 ABL was occupied by transported particulate matter with a high extinction coefficient and a low
487 depolarization ratio.

488 Due to the short time during the fixed-point observation period, it is difficult to make a universal
489 conclusion that no T-NEPS occurs in basin regions. Therefore, we further checked the surface and model
490 simulation data of the two basin cities for three months in winter 2018. We found that, unlike the plain
491 area, the T-NEPS events were rarely observed in the basin regions. It confirmed that the conceptual
492 model was indeed not applicable in the basin area. This was mainly attributed to the fact that the
493 movement of the weather system was blocked by the mountains surrounding the basin. Therefore, the
494 movement of the high-pressure system and the passage of the cold front had a weak impact on the basin
495 region. Without the downdrafts and the shift in wind direction associated with the movement of the high-
496 pressure system and the passage of the cold front, the structure of the ABL between Xi'an and Chengdu
497 was relatively stable, making it difficult for particulate matter to be transported and diffused, and thus
498 accumulate in the ABL at night. During the three months, we found that the wind field in Xi'an was
499 dominated by light winds, while in Chengdu there were two states: one was dominated by light winds
500 and the other by strong northeasterly winds. Fortunately, our fixed-point observations had captured these
501 typical processes indeed. In addition, considering the wind fields in basin cities were mainly dominated
502 by light winds, which was the main characteristic of basin area (Bei et al., 2016; Shu et al., 2021) and
503 was similar to the wind fields below 1,500 m in Taiyuan and Linfen of the Type 4. Therefore, we
504 suggested that the Loess Plateau cities might serve as a crucial transitional zone between the plains and
505 the basin as introduced in Section 3.3. In summary, the conceptual model of T-NPES events was
506 applicable to the plain areas which were more influenced by the movement of the weather system in
507 winter, such as the NCP and YRD, but not to the basin areas.



508

509 **Figure 8.** (a) Surface PM_{2.5} concentration and relative humidity, (b) Extinction coefficient, (c) Depolarization ratio,
 510 (d) Horizontal wind, and (e) Vertical wind, during the observation in Chengdu from 20:00, 7 January to 8:00, 10
 511 January. The two black boxes were the period of the double-layer structure, the orange box was the period to be
 512 studied.

513 **4 Conclusions and outlook**

514 In this study, we reveal that the T-NPES is a relatively common and important pathway that causes PM_{2.5}
 515 pollution in the surface layer in plain areas in winter China. The fixed-point observations in Changzhou
 516 and Wangdu demonstrated that the T-NPES was associated with the subsidence of particulate matter in
 517 the upper layer due to the movement of high pressure and the passage of the cold front. Model simulations
 518 further confirmed the ubiquity of T-NPES events in plain areas, despite these event types varied case by
 519 case. However, the observations in Xi'an and Chengdu indicated that the event was less occurred in the
 520 basin areas, as the impact of the weather system was weakened by the obstruction of mountains
 521 surrounding the basin. In future studies, more multi-lidar measurements should be conducted in other

522 cities in the plains and basin areas to look insight to the detailed mechanism of T-NPES events. In
523 addition, more works are urgently needed to uncover the vertical profiles of chemical components of the
524 particulate matter, since it may also be affected by the coupling of physical and chemical processes.

525 **Code/Data availability.** The datasets used in this study are available at:
526 <https://doi.org/10.5281/zenodo.8368944> (Wang et al., 2023).

527 **Author contributions.** H.C.W. and S.J.F designed the study. Y.M.W. and H.C.W. analyzed the data,
528 H.L.W. and X.L. provided the GEOS-Chem model simulation results, and Y.M.W. and H.C.W. wrote
529 the paper with input from all coauthors.

530 **Competing interests.** The authors declare that they have no conflicts of interest.

531 **Acknowledgments.** The authors gratefully acknowledge the NOAA Air Resources Laboratory (ARL)
532 for the provision of the HYSPLIT transport and dispersion model used in this study.

533 **Financial support.** This research has been supported by the Guangdong Major Project of Basic and
534 Applied Basic Research (grant no. 2020B0301030004), the National Research Program for Key Issue in
535 Air Pollution Control (grant no. 2023YFC3709201, 2023YFC3706103, 2023YFC3710900), and the
536 National Natural Science Foundation of China (grant no. 42175111), the Fundamental Research Funds
537 for the Central Universities, Sun Yat-sen University (23lgbj002).

538 **References**

539 An, Z.S., Huang, R.J., Zhang, R.Y., Tie, X.X., Li, G.H., Cao, J.J., Zhou, W.J., Shi, Z.G., Han, Y.M., Gu,
540 Z.L., Ji, Y.M.: Severe haze in northern China: A synergy of anthropogenic emissions and
541 atmospheric processes. *P. Natl. Acad. Sci. USA.* 116, 8657-8666.
542 <http://doi.org/10.1073/pnas.1900125116>, 2019

543 Bei, N.F., Xiao, B., Meng, N., Feng, T.: Critical role of meteorological conditions in a persistent haze
544 episode in the Guanzhong basin, China. *Sci. Total Environ.*, 550, 273-284.
545 <http://doi.org/10.1016/j.scitotenv.2015.12.159>, 2016

546 Bey, I., Jacob, D.J., Yantosca, R.M., Logan, J.A., Field, B.D., Fiore, A.M., Li, Q.B., Liu, H.G.Y.,
547 Mickley, L.J., Schultz, M.G.: Global modeling of tropospheric chemistry with assimilated

548 meteorology: Model description and evaluation. *J. Geophys. Res.: Atmos.*, 106, 23073-23095.
549 <http://doi.org/10.1029/2001JD000807>, 2001

550 Bian, H.S., Prather, M.J.: Fast-J2: Accurate simulation of stratospheric photolysis in global chemical
551 models. *J. Atmos. Chem.*, 41, 281-296. <http://doi.org/10.1023/A:1014980619462>, 2002

552 Cai, W.J., Li, K., Liao, H., Wang, H.J., Wu, L.X.: Weather conditions conducive to Beijing severe haze
553 more frequent under climate change. *Nat. Clim. Change.* 7, 257-+.
554 <http://doi.org/10.1038/NCLIMATE3249>, 2017

555 Callahan, C.W., Schnell, J.L., Horton, D.E.: Multi-Index Attribution of Extreme Winter Air Quality in
556 Beijing, China. *J. Geophys. Res.: Atmos.*, 124, 4567-4583.
557 <http://doi.org/10.1029/2018JD029738>, 2019

558 Carlson, M.A., Stull, R.B.: Subsidence in the nocturnal boundary layer. *J. Clim. Appl. Meteorol.*, 25,
559 1088-1099. [http://doi.org/10.1175/1520-0450\(1986\)025<1088:sitnbl>2.0.co;2](http://doi.org/10.1175/1520-0450(1986)025<1088:sitnbl>2.0.co;2), 1986

560 Chen, X.R., Wang, H.C., Lu, K.D., Li, C.M., Zhai, T.Y., Tan, Z.F., Ma, X.F., Yang, X.P., Liu, Y.H.,
561 Chen, S.Y., Dong, H.B., Li, X., Wu, Z.J., Hu, M., Zeng, L.M., Zhang, Y.H.: Field Determination
562 of Nitrate Formation Pathway in Winter Beijing. *Environ. Sci. Technol.*, 54, 9243-9253.
563 <http://doi.org/10.1021/acs.est.0c00972>, 2020

564 De Marco, A., Proietti, C., Anav, A., Ciancarella, L., D'Elia, I., Fares, S., Fornasier, M.F., Fusaro, L.,
565 Gualtieri, M., Manes, F., Marchetto, A., Mircea, M., Paoletti, E., Piersanti, A., Rogora, M.,
566 Salvati, L., Salvatori, E., Screpanti, A., Vialetto, G., Vitale, M., Leonardi, C.: Impacts of air
567 pollution on human and ecosystem health, and implications for the National Emission Ceilings
568 Directive: Insights from Italy. *Environ. Int.*, 125, 320-333.
569 <http://doi.org/10.1016/j.envint.2019.01.064>, 2019

570 Ding, A.J., Fu, C.B., Yang, X.Q., Sun, J.N., Petaja, T., Kerminen, V.M., Wang, T., Xie, Y., Herrmann,
571 E., Zheng, L.F., Nie, W., Liu, Q., Wei, X.L., Kulmala, M.: Intense atmospheric pollution
572 modifies weather: a case of mixed biomass burning with fossil fuel combustion pollution in
573 eastern China. *Atmos. Chem. Phys.*, 13, 10545-10554. [http://doi.org/10.5194/acp-13-10545-](http://doi.org/10.5194/acp-13-10545-2013)
574 [2013](http://doi.org/10.5194/acp-13-10545-2013), 2013

575 Ding, A.J., Huang, X., Nie, W., Chi, X.G., Xu, Z., Zheng, L.F., Xu, Z.N., Xie, Y.N., Qi, X.M., Shen,
576 Y.C., Sun, P., Wang, J.P., Wang, L., Sun, J.N., Yang, X.Q., Qin, W., Zhang, X.Z., Cheng, W.,
577 Liu, W.J., Pan, L.B., Fu, C.B.: Significant reduction of PM_{2.5} in eastern China due to regional-

578 scale emission control: evidence from SORPES in 2011-2018. *Atmos. Chem. Phys.*, 19, 11791-
579 11801. <http://doi.org/10.5194/acp-19-11791-2019>, 2019

580 Dong, Z.P., Li, Z.Q., Yu, X., Cribb, M., Li, X.M., Dai, J.: Opposite long-term trends in aerosols between
581 low and high altitudes: a testimony to the aerosol-PBL feedback. *Atmos. Chem. Phys.*, 17, 7997-
582 8009. <http://doi.org/10.5194/acp-17-7997-2017>, 2017

583 Dubey, R., Patra, A.K., Joshi, J., Blankenberg, D., Nazneen. Evaluation of vertical and horizontal
584 distribution of particulate matter near an urban roadway using an unmanned aerial vehicle. *Sci.*
585 *Total Environ.*, 836. <http://doi.org/10.1016/j.scitotenv.2022.155600>, 2022

586 Fast, J.D., Bell, D.M., Kulkarni, G., Liu, J.M., Mei, F., Saliba, G., Shilling, J.E., Suski, K., Tomlinson,
587 J., Wang, J., Zaveri, R., Zelenyuk, A.: Using aircraft measurements to characterize subgrid-
588 scale variability of aerosol properties near the Atmospheric Radiation Measurement Southern
589 Great Plains site. *Atmos. Chem. Phys.*, 22, 11217-11238. [http://doi.org/10.5194/acp-22-11217-
590 2022](http://doi.org/10.5194/acp-22-11217-2022), 2022

591 Gao, M., Carmichael, G.R., Wang, Y., Saide, P.E., Yu, M., Xin, J., Liu, Z., Wang, Z.: Modeling study
592 of the 2010 regional haze event in the North China Plain. *Atmos. Chem. Phys.*, 16, 1673-1691.
593 <http://doi.org/10.5194/acp-16-1673-2016>, 2016

594 Gao, M., Liu, Z.R., Zheng, B., Ji, D.S., Sherman, P., Song, S.J., Xin, J.Y., Liu, C., Wang, Y.S., Zhang,
595 Q., Xing, J., Jiang, J.K., Wang, Z.F., Carmichael, G.R., McElroy, M.B.: China's emission
596 control strategies have suppressed unfavorable influences of climate on wintertime PM_{2.5}
597 concentrations in Beijing since 2002. *Atmos. Chem. Phys.*, 20, 1497-1505.
598 <http://doi.org/10.5194/acp-20-1497-2020>, 2020

599 Gao, M., Saide, P.E., Xin, J.Y., Wang, Y.S., Liu, Z.R., Wang, Y.X., Wang, Z.F., Pagowski, M.,
600 Guttikunda, S.K., Carmichael, G.R.: Estimates of Health Impacts and Radiative Forcing in
601 Winter Haze in Eastern China through Constraints of Surface PM_{2.5} Predictions. *Environ. Sci.*
602 *Technol.*, 51, 2178-2185. <http://doi.org/10.1021/acs.est.6b03745>, 2017

603 Gelaro, R., McCarty, W., Suarez, M.J., Todling, R., Molod, A., Takacs, L., Randles, C.A., Darmenov,
604 A., Bosilovich, M.G., Reichle, R., Wargan, K., Coy, L., Cullather, R., Draper, C., Akella, S.,
605 Buchard, V., Conaty, A., da Silva, A.M., Gu, W., Kim, G.K., Koster, R., Lucchesi, R., Merkova,
606 D., Nielsen, J.E., Partyka, G., Pawson, S., Putman, W., Rienecker, M., Schubert, S.D.,
607 Sienkiewicz, M., Zhao, B.: The Modern-Era Retrospective Analysis for Research and

608 Applications, Version 2 (MERRA-2). *J. Clim.*, 30, 5419-5454. <http://doi.org/10.1175/JCLI-D->
609 [16-0758.1](http://doi.org/10.1175/JCLI-D-16-0758.1), 2017

610 Geng, G.N., Xiao, Q.Y., Liu, S.G., Liu, X.D., Cheng, J., Zheng, Y.X., Xue, T., Tong, D., Zheng, B.,
611 Peng, Y.R., Huang, X.M., He, K.B., Zhang, Q.: Tracking Air Pollution in China: Near Real-
612 Time PM_{2.5} Retrievals from Multisource Data Fusion. *Environ. Sci. Technol.*, 55, 12106-12115.
613 <http://doi.org/10.1021/acs.est.1c01863>, 2021a

614 Geng, G.N., Zheng, Y.X., Zhang, Q., Xue, T., Zhao, H.Y., Tong, D., Zheng, B., Li, M., Liu, F., Hong,
615 C.P., He, K.B., Davis, S.J.: Drivers of PM_{2.5} air pollution deaths in China 2002-2017. *Nat.*
616 *Geosci.*, 14, 645-+. <http://doi.org/10.1038/s41561-021-00792-3>, 2021b

617 Gramsch, E., Caceres, D., Oyola, P., Reyes, E., Vasquez, Y., Rubio, M.A., Sanchez, G.: Influence of
618 surface and subsidence thermal inversion on PM_{2.5} and black carbon concentration. *Atmos.*
619 *Environ.*, 98, 290-298. <http://doi.org/10.1016/j.atmosenv.2014.08.066>, 2014

620 Guo, S., Hu, M., Zamora, M.L., Peng, J.F., Shang, D.J., Zheng, J., Du, Z.F., Wu, Z., Shao, M., Zeng,
621 L.M., Molina, M.J., Zhang, R.Y.: Elucidating severe urban haze formation in China. *P. Natl.*
622 *Acad. Sci. USA.* 111, 17373-17378. <http://doi.org/10.1073/pnas.1419604111>, 2014

623 Hao, X., Li, J.D., Wang, H.J., Liao, H., Yin, Z.C., Hu, J.L., Wei, Y., Dang, R.J.: Long-term health impact
624 of PM_{2.5} under whole-year COVID-19 lockdown. *Environ. Pollut.*, 290.
625 <http://doi.org/10.1016/j.envpol.2021.118118>, 2021

626 He, C., Lu, X., Wang, H.L., Wang, H.C., Li, Y., He, G.W., He, Y.P., Wang, Y.R., Zhang, Y.L., Liu,
627 Y.M., Fan, Q., Fan, S.J.: The unexpected high frequency of nocturnal surface ozone
628 enhancement events over China: characteristics and mechanisms. *Atmos. Chem. Phys.*, 22,
629 15243-15261. <http://doi.org/10.5194/acp-22-15243-2022>, 2022

630 He, Y.P., Xu, X.Q., Gu, Z.L., Chen, X.H., Li, Y.M., Fan, S.J.: Vertical distribution characteristics of
631 aerosol particles over the Guanzhong Plain. *Atmos. Environ.*, 255.
632 <http://doi.org/10.1016/j.atmosenv.2021.118444>, 2021

633 Hu, X.-M., Klein, P.M., Xue, M., Zhang, F., Doughty, D.C., Forkel, R., Joseph, E., Fuentes, J.D.: Impact
634 of the vertical mixing induced by low-level jets on boundary layer ozone concentration. *Atmos.*
635 *Environ.*, 70, 123-130. <http://doi.org/10.1016/j.atmosenv.2012.12.046>, 2013

636 Huang, R.J., Zhang, Y.L., Bozzetti, C., Ho, K.F., Cao, J.J., Han, Y.M., Daellenbach, K.R., Slowik, J.G.,
637 Platt, S.M., Canonaco, F., Zotter, P., Wolf, R., Pieber, S.M., Bruns, E.A., Crippa, M., Ciarelli,
638 G., Piazzalunga, A., Schwikowski, M., Abbaszade, G., Schnelle-Kreis, J., Zimmermann, R., An,

639 Z.S., Szidat, S., Baltensperger, U., El Haddad, I., Prevot, A.S.H.: High secondary aerosol
640 contribution to particulate pollution during haze events in China. *Nature*. 514, 218-222.
641 <http://doi.org/10.1038/nature13774>, 2014

642 Huang, X., Ding, A.J., Wang, Z.L., Ding, K., Gao, J., Chai, F.H., Fu, C.B.: Amplified transboundary
643 transport of haze by aerosol-boundary layer interaction in China. *Nat. Geosci.*, 13, 428-+.
644 <http://doi.org/10.1038/s41561-020-0583-4>, 2020

645 Huang, X., Wang, Z.L., Ding, A.J.: Impact of Aerosol-PBL Interaction on Haze Pollution: Multiyear
646 Observational Evidences in North China. *Geophys. Res. Lett.*, 45, 8596-8603.
647 <http://doi.org/10.1029/2018GL079239>, 2018

648 Kang, H.Q., Zhu, B., Gao, J.H., He, Y., Wang, H.L., Su, J.F., Pan, C., Zhu, T., Yu, B.: Potential impacts
649 of cold frontal passage on air quality over the Yangtze River Delta, China. *Atmos. Chem. Phys.*,
650 19, 3673-3685. <http://doi.org/10.5194/acp-19-3673-2019>, 2019

651 Kang, H.Q., Zhu, B., Liu, X.H., Shi, S.S., Hou, X.W., Lu, W., Yan, S.Q., Pan, C., Chen, Y.: Three-
652 Dimensional Distribution of PM_{2.5} over the Yangtze River Delta as Cold Fronts Moving
653 Through. *J. Geophys. Res.: Atmos.*, 126. <http://doi.org/10.1029/2020JD034035>, 2021

654 Kraus, H., Malcher, J., Schaller, E.: A nocturnal low level jet during PUKK. *Bound.-Layer Meteorol.*
655 (Netherlands). 31, 187-195. <http://doi.org/10.1007/bf00121177>, 1985

656 Largeron, Y., Staquet, C.: Persistent inversion dynamics and wintertime PM₁₀ air pollution in Alpine
657 valleys. *Atmos. Environ.*, 135, 92-108. <http://doi.org/10.1016/j.atmosenv.2016.03.045>, 2016

658 Li, H.Y., Cheng, J., Zhang, Q., Zheng, B., Zhang, Y.X., Zheng, G.J., He, K.B.: Rapid transition in winter
659 aerosol composition in Beijing from 2014 to 2017: response to clean air actions. *Atmos. Chem.*
660 *Phys.*, 19, 11485-11499. <http://doi.org/10.5194/acp-19-11485-2019>, 2019a

661 Li, L., Lu, C., Chan, P.W., Lan, Z.J., Zhang, W.H., Yang, H.L., Wang, H.C.: Impact of the COVID-19
662 on the vertical distributions of major pollutants from a tower in the Pearl River Delta. *Atmos.*
663 *Environ.*, 276. <http://doi.org/10.1016/j.atmosenv.2022.119068>, 2022

664 Li, Z.Q., Guo, J.P., Ding, A.J., Liao, H., Liu, J.J., Sun, Y.L., Wang, T.J., Xue, H.W., Zhang, H.S., Zhu,
665 B.: Aerosol and boundary-layer interactions and impact on air quality. *Natl. Sci. Rev.*, 4, 810-
666 833. <http://doi.org/10.1093/nsr/nwx117>, 2017

667 Li, Z.Q., Wang, Y., Guo, J.P., Zhao, C.F., Cribb, M., Dong, X.Q., Fan, J.W., Gong, D.Y., Huang, J.P.,
668 Jiang, M.J., Jiang, Y.Q., Lee, S.S., Li, H., Li, J.M., Liu, J.J., Qian, Y., Rosenfeld, D., Shan, S.Y.,
669 Sun, Y.L., Wang, H.J., Xin, J.Y., Yan, X., Yang, X., Yang, X.Q., Zhang, F., Zheng, Y.T.: East

670 Asian Study of Tropospheric Aerosols and their Impact on Regional Clouds, Precipitation, and
671 Climate (EAST-AIR(CPC)). *J. Geophys. Res.: Atmos.*, 124, 13026-13054.
672 <http://doi.org/10.1029/2019JD030758>, 2019b

673 Lin, J.T., McElroy, M.B.: Impacts of boundary layer mixing on pollutant vertical profiles in the lower
674 troposphere: Implications to satellite remote sensing. *Atmos. Environ.*, 44, 1726-1739.
675 <http://doi.org/10.1016/j.atmosenv.2010.02.009>, 2010

676 Lu, K.D., Fuchs, H., Hofzumahaus, A., Tan, Z.F., Wang, H.C., Zhang, L., Schmitt, S.H., Rohrer, F.,
677 Bohn, B., Broch, S., Dong, H.B., Gkatzelis, G.I., Hohaus, T., Holland, F., Li, X., Liu, Y., Liu,
678 Y.H., Ma, X.F., Novelli, A., Schlag, P., Shao, M., Wu, Y.S., Wu, Z.J., Zeng, L.M., Hu, M.,
679 Kiendler-Scharr, A., Wahner, A., Zhang, Y.H.: Fast Photochemistry in Wintertime Haze:
680 Consequences for Pollution Mitigation Strategies. *Environ. Sci. Technol.*, 53, 10676-10684.
681 <http://doi.org/10.1021/acs.est.9b02422>, 2019

682 Lv, L., Xiang, Y., Zhang, T., Chai, W., Liu, W.: Comprehensive study of regional haze in the North
683 China Plain with synergistic measurement from multiple mobile vehicle-based lidars and a lidar
684 network. *Sci. Total Environ.*, 721. <http://doi.org/10.1016/j.scitotenv.2020.137773>, 2020

685 Mao, J., Fan, S., Jacob, D.J., Travis, K.R.: Radical loss in the atmosphere from Cu-Fe redox coupling in
686 aerosols. *Atmos. Chem. Phys.*, 13, 509-519. <http://doi.org/10.5194/acp-13-509-2013>, 2013

687 Munoz-Sabater, J., Dutra, E., Agustí-Panareda, A., Albergel, C., Arduini, G., Balsamo, G., Boussetta, S.,
688 Choulga, M., Harrigan, S., Hersbach, H., Martens, B., Miralles, D.G., Piles, M., Rodríguez-
689 Fernández, N.J., Zsoter, E., Buontempo, C., Thepaut, J.N.: ERA5-Land: a state-of-the-art global
690 reanalysis dataset for land applications. *Earth Syst. Sci. Data.* 13, 4349-4383.
691 <http://doi.org/10.5194/essd-13-4349-2021>, 2021

692 O'Rourke, P.R., Smith, S.J., Mott, A., Ahsan, H., McDuffie, E.E., Crippa, M., Klimont, S., McDonald,
693 B., Z., W., Nicholson, M.B., Feng, L., Hoesly, R.M., 2021. CEDS v-2021-04-21 Emission Data
694 1975-2019 (Version Apr-21-2021).

695 Park, R.J., Jacob, D.J., Field, B.D., Yantosca, R.M., Chin, M.: Natural and transboundary pollution
696 influences on sulfate-nitrate-ammonium aerosols in the United States: Implications for policy.
697 *J. Geophys. Res.: Atmos.*, 109. <http://doi.org/10.1029/2003JD004473>, 2004

698 Parrella, J.P., Jacob, D.J., Liang, Q., Zhang, Y., Mickley, L.J., Miller, B., Evans, M.J., Yang, X., Pyle,
699 J.A., Theys, N., Van Roozendaal, M.: Tropospheric bromine chemistry: implications for present

700 and pre-industrial ozone and mercury. *Atmos. Chem. Phys.*, 12, 6723-6740.
701 <http://doi.org/10.5194/acp-12-6723-2012>, 2012

702 Peng, J.F., Hu, M., Shang, D.J., Wu, Z.J., Du, Z.F., Tan, T.Y., Wang, Y.N., Zhang, F., Zhang, R.Y.:
703 Explosive Secondary Aerosol Formation during Severe Haze in the North China Plain. *Environ.*
704 *Sci. Technol.*, 55, 2189-2207. <http://doi.org/10.1021/acs.est.0c07204>, 2021

705 Qin, Y., Li, J.Y., Gong, K.J., Wu, Z.J., Chen, M.D., Qin, M.M., Huang, L., Hu, J.L.: Double high
706 pollution events in the Yangtze River Delta from 2015 to 2019: Characteristics, trends, and
707 meteorological situations. *Sci. Total Environ.*, 792.
708 <http://doi.org/10.1016/j.scitotenv.2021.148349>, 2021

709 Ran, L., Deng, Z.Z., Wu, Y.F., Li, J.W., Bai, Z.X., Lu, Y., Zhuoga, D.Q., Bian, J.C.: Measurement report:
710 Vertical profiling of particle size distributions over Lhasa, Tibet - tethered balloon-based in situ
711 measurements and source apportionment. *Atmos. Chem. Phys.*, 22, 6217-6229.
712 <http://doi.org/10.5194/acp-22-6217-2022>, 2022

713 Shi, Y., Zeng, Q.C., Liu, L., Huo, J.T., Zhang, Z., Ding, W.C., Hu, F.: Observed Evidence That
714 Subsidence Process Stabilizes the Boundary Layer and Increases the Ground Concentration of
715 Secondary Pollutants. *J. Geophys. Res.: Atmos.*, 127. <http://doi.org/10.1029/2021JD035244>,
716 2022

717 Shu, Z.Z., Liu, Y.B., Zhao, T.L., Xia, J.R., Wang, C.G., Cao, L., Wang, H.L., Zhang, L., Zheng, Y., Shen,
718 L.J., Luo, L., Li, Y.Q.: Elevated 3D structures of PM_{2.5} and impact of complex terrain-forcing
719 circulations on heavy haze pollution over Sichuan Basin, China. *Atmos. Chem. Phys.*, 21, 9253-
720 9268. <http://doi.org/10.5194/acp-21-9253-2021>, 2021

721 Silver, B., Conibear, L., Reddington, C.L., Knote, C., Arnold, S.R., Spracklen, D.V.: Pollutant emission
722 reductions deliver decreased PM_{2.5}-caused mortality across China during 2015-2017. *Atmos.*
723 *Chem. Phys.*, 20, 11683-11695. <http://doi.org/10.5194/acp-20-11683-2020>, 2020

724 Song, R.F., Wang, D.S., Li, X.B., Li, B., Peng, Z.R., He, H.D.: Characterizing vertical distribution
725 patterns of PM_{2.5} in low troposphere of Shanghai city, China: Implications from the perspective
726 of unmanned aerial vehicle observations. *Atmos. Environ.*, 265.
727 <http://doi.org/10.1016/j.atmosenv.2021.118724>, 2021

728 Stein, A.F., Draxler, R.R., Rolph, G.D., Stunder, B.J.B., Cohen, M.D., Ngan, F.: NOAA'S HYSPLIT
729 ATMOSPHERIC TRANSPORT AND DISPERSION MODELING SYSTEM. *Bull. Am.*
730 *Meteorol. Soc.*, 96, 2059-2077. <http://doi.org/10.1175/BAMS-D-14-00110.1>, 2015

- 731 Wang, D.F., Huo, J.T., Duan, Y.S., Zhang, K., Ding, A.J., Fu, Q.Y., Luo, J.H., Fei, D.N., Xiu, G.L.,
732 Huang, K.: Vertical distribution and transport of air pollutants during a regional haze event in
733 eastern China: A tethered mega-balloon observation study. *Atmos. Environ.*, 246.
734 <http://doi.org/10.1016/j.atmosenv.2020.118039>, 2021
- 735 Wang, F., Li, Z.Q., Ren, X.R., Jiang, Q., He, H., Dickerson, R.R., Dong, X.B., Lv, F.: Vertical
736 distributions of aerosol optical properties during the spring 2016 ARIAs airborne campaign in
737 the North China Plain. *Atmos. Chem. Phys.*, 18, 8995-9010. [http://doi.org/10.5194/acp-18-](http://doi.org/10.5194/acp-18-8995-2018)
738 [8995-2018](http://doi.org/10.5194/acp-18-8995-2018), 2018
- 739 Wang, H.C., Lu, K.D., Chen, X.R., Zhu, Q.D., Chen, Q., Guo, S., Jiang, M.Q., Li, X., Shang, D.J., Tan,
740 Z.F., Wu, Y.S., Wu, Z.J., Zou, Q., Zheng, Y., Zeng, L.M., Zhu, T., Hu, M., Zhang, Y.H.: High
741 N₂O₅ Concentrations Observed in Urban Beijing: Implications of a Large Nitrate Formation
742 Pathway. *Environ. Sci. Technol. Lett.*, 4, 416-420. <http://doi.org/10.1021/acs.estlett.7b00341>,
743 2017
- 744 Wang, H.C., Wang, H.L., Lu, X., Lu, K.D., Zhang, L., Tham, Y.J., Shi, Z.B., Aikin, K., Fan, S.J., Brown,
745 S.S., Zhang, Y.H.: Increased night-time oxidation over China despite widespread decrease
746 across the globe. *Nat. Geosci.*, 16, 217-+. <http://doi.org/10.1038/s41561-022-01122-x>, 2023
- 747 Wang, Y.H., Logan, J.A., Jacob, D.J.: Global simulation of tropospheric O₃-NO_x-hydrocarbon
748 chemistry. 2. Model evaluation and global ozone budget. *J. Geophys. Res. (USA)*. 103, 10727-
749 10755. <http://doi.org/10.1029/98jd00157>, 1998
- 750 Wesely, M.L.: Parameterization of surface resistances to gaseous dry deposition in regional-scale
751 numerical models. *Atmos. Environ.*, 23, 1293-1304. [http://doi.org/10.1016/0004-](http://doi.org/10.1016/0004-6981(89)90153-4)
752 [6981\(89\)90153-4](http://doi.org/10.1016/0004-6981(89)90153-4), 1989
- 753 WHO. WHO Global Air Quality Guidelines: Particulate Matter (PM_{2.5} and PM₁₀), Ozone, Nitrogen
754 Dioxide, Sulfur Dioxide and Carbon Monoxide, World Health Organization (WHO), Geneva,
755 Switzerland., 2021
- 756 Xiao, Q.Y., Geng, G.N., Cheng, J., Liang, F.C., Li, R., Meng, X., Xue, T., Huang, X.M., Kan, H.D.,
757 Zhang, Q., He, K.B.: Evaluation of gap-filling approaches in satellite-based daily PM_{2.5}
758 prediction models. *Atmos. Environ.*, 244. <http://doi.org/10.1016/j.atmosenv.2020.117921>,
759 2021a
- 760 Xiao, Q.Y., Zheng, Y.X., Geng, G.N., Chen, C.H., Huang, X.M., Che, H.Z., Zhang, X.Y., He, K.B.,
761 Zhang, Q.: Separating emission and meteorological contributions to long-term PM_{2.5} trends over

762 eastern China during 2000-2018. *Atmos. Chem. Phys.*, 21, 9475-9496.
763 <http://doi.org/10.5194/acp-21-9475-2021>, 2021b

764 Xu, X.Q., Xie, J.L., Li, Y.M., Miao, S.J., Fan, S.J.: Measurement report: Vehicle-based multi-lidar
765 observational study of the effect of meteorological elements on the three-dimensional
766 distribution of particles in the western Guangdong-Hong Kong-Macao Greater Bay Area.
767 *Atmos. Chem. Phys.*, 22, 139-153. <http://doi.org/10.5194/acp-22-139-2022>, 2022

768 Xu, Z.N., Huang, X., Nie, W., Shen, Y.C., Zheng, L.F., Xie, Y.N., Wang, T.Y., Ding, K., Liu, L.X.,
769 Zhou, D.R., Qi, X.M., Ding, A.J.: Impact of Biomass Burning and Vertical Mixing of Residual-
770 Layer Aged Plumes on Ozone in the Yangtze River Delta, China: A Tethered-Balloon
771 Measurement and Modeling Study of a Multiday Ozone Episode. *J. Geophys. Res.: Atmos.*,
772 123, 11786-11803. <http://doi.org/10.1029/2018JD028994>, 2018

773 Yan, C., Tham, Y.J., Nie, W., Xia, M., Wang, H.C., Guo, Y.S., Ma, W., Zhan, J.L., Hua, C.J., Li, Y.Y.,
774 Deng, C.J., Li, Y.R., Zheng, F.X., Chen, X., Li, Q.Y., Zhang, G., Mahajan, A.S., Cuevas, C.A.,
775 Huang, D.D., Wang, Z., Sun, Y.L., Saiz-Lopez, A., Bianchi, F., Kerminen, V.M., Worsnop,
776 D.R., Donahue, N.M., Jiang, J.K., Liu, Y.C., Ding, A.J., Kulmala, M.: Increasing contribution
777 of nighttime nitrogen chemistry to wintertime haze formation in Beijing observed during
778 COVID-19 lockdowns. *Nat. Geosci.*, 16, 975-+. <http://doi.org/10.1038/s41561-023-01285-1>,
779 2023

780 Yin, C.Q., Xu, J.M., Gao, W., Pan, L., Gu, Y.X., Fu, Q.Y., Yang, F.: Characteristics of fine particle
781 matter at the top of Shanghai Tower. *Atmos. Chem. Phys.*, 23, 1329-1343.
782 <http://doi.org/10.5194/acp-23-1329-2023>, 2023

783 Yue, X., Unger, N., Harper, K., Xia, X.G., Liao, H., Zhu, T., Xiao, J.F., Feng, Z.Z., Li, J.: Ozone and
784 haze pollution weakens net primary productivity in China. *Atmos. Chem. Phys.*, 17, 6073-6089.
785 <http://doi.org/10.5194/acp-17-6073-2017>, 2017

786 Zhang, G., Gao, Y., Cai, W.J., Leung, L.R., Wang, S.X., Zhao, B., Wang, M.H., Shan, H.Y., Yao, X.H.,
787 Gao, H.W.: Seesaw haze pollution in North China modulated by the sub-seasonal variability of
788 atmospheric circulation. *Atmos. Chem. Phys.*, 19, 565-576. [http://doi.org/10.5194/acp-19-565-](http://doi.org/10.5194/acp-19-565-2019)
789 [2019](http://doi.org/10.5194/acp-19-565-2019), 2019a

790 Zhang, L.M., Gong, S.L., Padro, J., Barrie, L.: A size-segregated particle dry deposition scheme for an
791 atmospheric aerosol module. *Atmos. Environ.*, 35, 549-560. [http://doi.org/10.1016/S1352-](http://doi.org/10.1016/S1352-2310(00)00326-5)
792 [2310\(00\)00326-5](http://doi.org/10.1016/S1352-2310(00)00326-5), 2001

793 Zhang, Q., Zheng, Y.X., Tong, D., Shao, M., Wang, S.X., Zhang, Y.H., Xu, X.D., Wang, J.N., He, H.,
794 Liu, W.Q., Ding, Y.H., Lei, Y., Li, J.H., Wang, Z.F., Zhang, X.Y., Wang, Y.S., Cheng, J., Liu,
795 Y., Shi, Q.R., Yan, L., Geng, G.N., Hong, C.P., Li, M., Liu, F., Zheng, B., Cao, J.J., Ding, A.J.,
796 Gao, J., Fu, Q.Y., Huo, J.T., Liu, B.X., Liu, Z.R., Yang, F.M., He, K.B., Hao, J.M.: Drivers of
797 improved PM_{2.5} air quality in China from 2013 to 2017. *P. Natl. Acad. Sci. USA.* 116, 24463-
798 24469. <http://doi.org/10.1073/pnas.1907956116>, 2019b

799 Zhang, R.Y., Wang, G.H., Guo, S., Zarnora, M.L., Ying, Q., Lin, Y., Wang, W.G., Hu, M., Wang, Y.:
800 Formation of Urban Fine Particulate Matter. *Chem. Rev.*, 115, 3803-3855.
801 <http://doi.org/10.1021/acs.chemrev.5b00067>, 2015

802 Zhang, W.H., Li, W.S., An, X.D., Zhao, Y.H., Sheng, L.F., Hai, S.F., Li, X.D., Wang, F., Zi, Z.F., Chu,
803 M.: Numerical study of the amplification effects of cold-front passage on air pollution over the
804 North China Plain. *Sci. Total Environ.*, 833. <http://doi.org/10.1016/j.scitotenv.2022.155231>,
805 2022

806 Zhao, X.J., Zhao, P.S., Xu, J., Meng, W., Pu, W.W., Dong, F., He, D., Shi, Q.F.: Analysis of a winter
807 regional haze event and its formation mechanism in the North China Plain. *Atmos. Chem. Phys.*,
808 13, 5685-5696. <http://doi.org/10.5194/acp-13-5685-2013>, 2013

809 Zhao, X.X., Zhao, X.J., Liu, P.F., Chen, D., Zhang, C.L., Xue, C.Y., Liu, J.F., Xu, J., Mu, Y.J.: Transport
810 Pathways of Nitrate Formed from Nocturnal N₂O₅ Hydrolysis Aloft to the Ground Level in
811 Winter North China Plain. *Environ. Sci. Technol.* <http://doi.org/10.1021/acs.est.3c00086>, 2023

812 Zheng, B., Tong, D., Li, M., Liu, F., Hong, C.P., Geng, G.N., Li, H.Y., Li, X., Peng, L.Q., Qi, J., Yan,
813 L., Zhang, Y.X., Zhao, H.Y., Zheng, Y.X., He, K.B., Zhang, Q.: Trends in China's
814 anthropogenic emissions since 2010 as the consequence of clean air actions. *Atmos. Chem.*
815 *Phys.*, 18, 14095-14111. <http://doi.org/10.5194/acp-18-14095-2018>, 2018

816 Zhou, X., Huang, X., Sun, P., Chi, X., Ren, C., Lai, S., Wang, Z., Qi, X., Wang, J., Nie, W., Xu, Z., Huo,
817 J., Fu, Q., Ding, A.: Fast Secondary Aerosol Formation in Residual Layer and Its Impact on Air
818 Pollution Over Eastern China. *J. Geophys. Res.: Atmos.*, 128, e2023JD038501.
819 <http://doi.org/https://doi.org/10.1029/2023JD038501>, 2023

820